PAPER

Check for updates

A synergistic co-passivation strategy for high-performance perovskite solar cells with large open circuit voltage†

Yan Feng, Rong Liu, Fumin Li, [iD] * Mengqi Jin, Qing Du, Yanjing Rong, Hangyu Hu, Mengxin Wang, Yu Li, Zhitao Shen, [iD] Ying Liu, Huilin Li [iD] and Chong Chen [iD]

Perovskite solar cells (PSCs) have shown great application potential due to their excellent performance and simple manufacturing processes. However, defects in the interior and surface of perovskite films are one of the vital issues restricting their further performance improvement. Therefore, it is imperative to reduce these defects. Here, we have developed a synergistic co-passivation strategy, which is a two-step targeted passivation (TSTP) sequentially using functional oleyl amine-coated MAPbBr$_3$ quantum-dot (M-QD) solution for the first step and n-octylammonium iodide (OAI) solution for the second step to treat the perovskite layer, in order to minimize defects in the perovskite film. According to the morphology, structure and photoelectric property measurements of the perovskite film, it has been revealed that the grain boundaries would be caulked by M-QDs and become fuzzy due to the DMF present in the M-QD solution. Further, the film defect passivation could be realized using OAI. As a result, the optimized TSTP-based PSC achieved an excellent power conversion efficiency of 22.01% with a high open-circuit voltage of 1.20 V and exhibited remarkable stability both in air ($\sim$25 °C at $\sim$30% humidity) and in an N$_2$ environment (at 85 °C or under continuous illumination), which are much better than those of the control PSC without any post-passivation.

1 Introduction

Organic–inorganic perovskite solar cells (PSCs) have attracted extensive attention because of their low-cost fabrication, solution processability and high power conversion efficiency (PCE).[1–4] To date, the rapidly increasing PCE of PSCs has reached 25.7% from an initial 3.8%,[5,6] which is mainly attributed to the unique properties of perovskite materials (ABX$_3$; A, B, and C are occupied by monovalent cations including CH$_3$NH$_3$$^+$(MA$^+$), HC(NH$_2$)$_2$$^+$(FA$^+$), Cs$^+$, divalent metal cations such as Pb^{2+} and Sn^{2+} and halogen anions including I$^-$, Br$^-$ and Cl$^-$), such as long carrier diffusion lengths and high optical absorption coefficients.[7–9] However, there is still a certain range of improvement relative to the theoretical Shockley–Queisser limit ($\sim$33%).[10,11] One of the most restrictive factors is the unavoidable result in numerous shallow level defects (such as the iodide and monovalent cation vacancy (V_I, V_{MA}, V_{FA}, *etc.*)) and deep level defects (such as monovalent and

iodide antisite substitutions (MA$_I$$^+$, FA$_I$$^+$, I$_{MA}$$^+$, I$_{FA}$$^+$, *etc.*) and uncoordinated Pb^{2+}) in perovskite films while using the traditional solution process,[1,12] leading to a large number of carrier complex centers and causing degradation in the performance of PSCs.[13] To overcome this issue, an effective way is to produce single-crystal PSCs. Nevertheless, immature processes and high cost of single-crystal PSCs are not suitable for the needs of sustainable development. Another widely used strategy is to use post-passivation treatment for minimizing the defects.

In recent years, a large number of functional materials, such as PMMA,[14,15] AQ310,[16] DMIMPF6 ionic liquid[17] and polyTPD,[18] have been used to passivate the defects of the perovskite absorber layer, resulting in more efficient and stable PSCs. In addition, some passivation processes are effective techniques to reduce the perovskite defects of PSCs prepared by the one-step anti-solvent method. First, a small amount of passivation materials, including CsPbBr$_3$ NPs,[19] TIPD,[20] TFBA[21] and ^{t}BP,[22] is added into the anti-solvent to passivate the perovskite film in the near-surface region during its crystallization. Second, to reduce surface defects, trace additives that can decompose perovskites such as DMF,[23,24] DMSO[25,26] and H$_2$O[27] are added into the post-treatment solvent for a recrystallization of the annealed perovskite film at the surface by a solvent-treatment process. Third, single organic ammonium iodides, including PEAI,[28–30] BAI,[31,32] or OAI,[33,34]

Henan Key Laboratory of Photovoltaic Materials, Henan University, Kaifeng 475004, P. R. China. E-mail: lifm@henu.edu.cn, leehl@henu.edu.cn, chongchen@henu.edu.cn

† Electronic supplementary information (ESI) available. See DOI: https://doi.org/10.1039/d2tc02632e

This journal is © The Royal Society of Chemistry 2022

J. Mater. Chem. C, 2022, **10**, 12699–12707 | **12699**

Fig. 1 (a) Device structure diagram and (b) cross-sectional SEM images of the PSCs.

are adopted to form 2D perovskites for defect passivation at the surface and/or grain boundaries and also by post-treatment. However, there is always just one material or one treatment process used for passivation, leading to incomplete defect repair simultaneously at the surface and grain boundaries and in the near-surface region of perovskite films.[13] Therefore, synergistic targeted co-passivation may be an effective strategy to overcome the incomplete repair issue.

Herein, we report a two-step targeted passivation (TSTP) strategy using functional oleyl amine (OLA)-coated $MAPbBr_3$ quantum-dots (denoted as M-QDs) and n-octylammonium iodide (OAI) solution for perovskite film passivation sequentially. The prepared n-i-p planar PSCs are based on $Cs_{0.05}(FA_{0.85}MA_{0.15})_{0.95}Pb(I_{0.85}Br_{0.15})_3$ (abbreviated as CFM), and the device structure is shown in Fig. 1a. The perovskite films are recrystallized in the near-surface region and caulked at grain boundaries by the functional M-QD solution treatment and then passivated at the surface by OAI. The results demonstrate that a trace amount of DMF contained in the M-QD solution is advantageous to dissolve and recrystallize the skin layer of the perovskite film. In addition, M-QDs will gather at the grain boundary and block moisture/oxygen *via* the coated functional OLA.[23,24,35,36] Moreover, OAI will interact with the surface

perovskite to form wrinkly two-dimensional perovskite,[33] leading to a defect-minimized perovskite film. Consequently, the optimized PSC by the TSTP strategy shows a higher PCE (22.01%) than that of the control one (18.97%) and displays an excellent open-circuit voltage (V_{oc}) of 1.20 V. Moreover, the un-encapsulated PSCs demonstrate good operational stabilities, maintaining 75% (or 80%) and 90% of their pristine efficiency storage in an N_2 atmosphere for up to 2000 h at 85 °C (or 1000 h under continuous illumination) and in ambient conditions ($\sim$25 °C at $\sim$30% humidity) for over 2000 h, respectively.

2. Results and discussion

As shown in Fig. 1b, the thickness of each layer in the PSCs measured by cross-sectional scanning electron microscopy (SEM) characterization is about 40, 500, 170 and 80 nm for SnO_2–KCl, CFM, Spiro-OMeTAD and Au, respectively, while the M-QD and OAI layers are too thin to be clearly observed. However, it can be seen from Fig. 2c that the obvious changes on the surface of the perovskite films happened after the M-QD and OAI treatment (denoted as TSTP-CFM) as compared with the untreated ones (Fig. 2a). On the one hand, the M-QDs are caulked at the grain boundaries of the perovskite film, which also can be clearly seen from SEM of the only M-QDs treatement film as shown in Fig. S1a (ESI†). And the grain boundaries become fuzzy because a trace amount of DMF contained in the M-QD solution is advantageous to dissolve and recrystallize the perovskite film.[24] On the other hand, a large number of nano-wrinkles are formed on the surface of perovskite grains, which is beneficial to the PCE improvement of PSCs due to the amelioration of the charge separation efficiency by the increased contact area between the perovskite and hole transport material (HTM).[37] The nano-wrinkles also appeared on the perovskite film treated only by OAI (Fig. S1b, ESI†). To understand the morphology and properties of M-QDs, transmission electron microscopy (TEM), X-ray diffraction (XRD) and ultraviolet-visible (UV-vis) measurements were performed (Fig. S2, ESI†). Fig. 2b and d show that the surface root-mean-square (RMS) roughness is reduced to 13.0 nm for the TSTP-CFM film from 25.9 nm for the control one, confirming a smoother perovskite film treated by TSTP.[38] In brief, the perovskite surface and grain boundary were repaired by the TSTP method, leading to a highly efficient device.
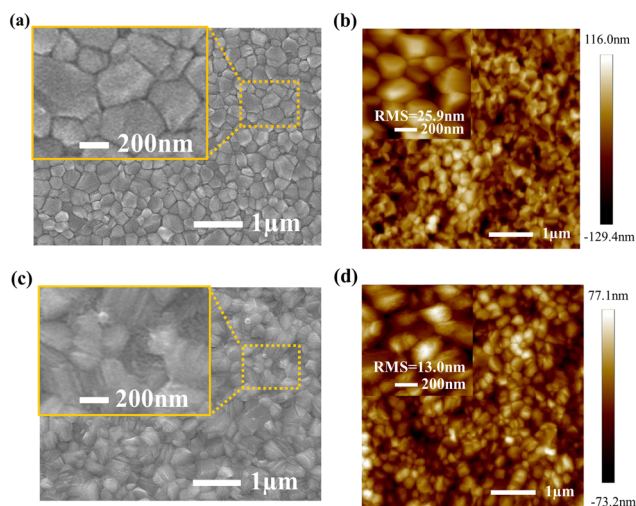

Fig. 2 Top-views of (a) SEM and (b) AFM images of the control CFM film. Top-views of (c) SEM and (d) AFM images of the TSTP-CFM film.

12700 | *J. Mater. Chem. C*, 2022, **10**, 12699–12707

This journal is © The Royal Society of Chemistry 2022

XRD patterns were analyzed to confirm the structure of the as-synthesized perovskite films (Fig. 3a). It can be seen that both films of the control CFM and TSTP-CFM exhibit (1 0 0), (1 1 0), (1 1 1) and (2 0 0) structures at 14.0°, 20.0°, 24.5° and 28.4° 2θ angles, respectively, agreeing well with the reported results,[39] which indicate that TSTP did not change the crystal structure. However, the diffraction intensity of the TSTP-CFM film increased significantly, especially, at 14.0° and 28.4° 2θ angles, indicating an improved crystallinity of the film. Similar results were also observed in the XRD patterns of the perovskite films treated only with the M-QD or OAI solution (Fig. S3, ESI†).

To investigate the optical and electrical properties of the perovskite films, UV-vis absorption spectroscopy, steady-state and time-resolved photoluminescence (PL and TRPL) and transient photovoltage decay (TPV) measurements were conducted. The UV-vis absorption spectra (Fig. 3b) show that the TSTP treatment does not affect the absorption edge with an approximate band gap of 1.62 eV but increased the absorption intensity in the whole visible range of the perovskite films, which is due to the contribution of TSTP-CFM with better crystallinity (Fig. 3a).[40,41] The higher the absorption intensity, larger short circuit current density (J_{sc}) may be obtained. The UV-vis absorption spectra of CFM treated only with M-QDs or OAI are also obtained as shown in Fig. S4 (ESI†), demonstrating the equal band gap of 1.62 eV. Moreover, PL curves (Fig. 3b) show the same luminescence peaks at 770 nm, matching well with the UV-vis absorption curves. However, the PL intensity of

the TSTP-CFM film is much higher than that of the control one. Moreover, the TRPL decay curves (Fig. 3c) show that the carrier average lifetime (τ_{avg}) for the TSTP-CFM film (5.72 µs) is longer than that of the control one (5.72 µs). The fitting details, with the two-component exponential decay for the TRPL are summarized in Table S1 (ESI†). The higher PL intensity and longer τ_{avg} imply suppressed nonradiative charge recombination *via* fewer defects on the surface and/or along the grain boundaries.[13,42] The fewer defects of TSTP-CFM film can also be confirmed from the longer charge-carrier recombination lifetime shown in the TPV measurements (Fig. 3d).[43] So that it is expected to obtain an excellent performance PSC device while using TSTP-CFM film.

All the devices are prepared with the planar heterojunction configuration of ITO/SnO$_2$–KCl/KF/perovskite (with/without post-treatment)/sprio-OMeTAD/Au (Fig. 1a) *via* a one-step anti-solvent method. The details are described in the Experimental Section. Fig. 4a and Table 1 depict the current density–voltage (J–V) characteristics of the devices fabricated with/without using TSTP. The TSTP device displays good photovoltaic properties with a PCE of 22.01% (a V_{oc} of 1.20 V, a J_{sc} of 24.79 mA cm^{-2} and a fill factor (FF) of 0.74) under forward scans (FS) and 21.04% (a V_{oc} of 1.20 V, a J_{sc} of 24.7 mA cm^{-2} and a FF of 0.71) under reverse scans (RS). Compared with the PCE of 18.97% under FS and 17.61% under RS of the control device, the PCE of the TSTP device increased significantly. The statistical distribution for the performance parameters of both the types of

Fig. 3 (a) XRD patterns, (b) UV–vis absorption spectra and steady-state PL (excited at 515 nm, the inset shows their band gaps) and (c) TRPL of the control CFM and TSTP-CFM films. (d) TPV of the control CFM and TSTP-CFM devices.
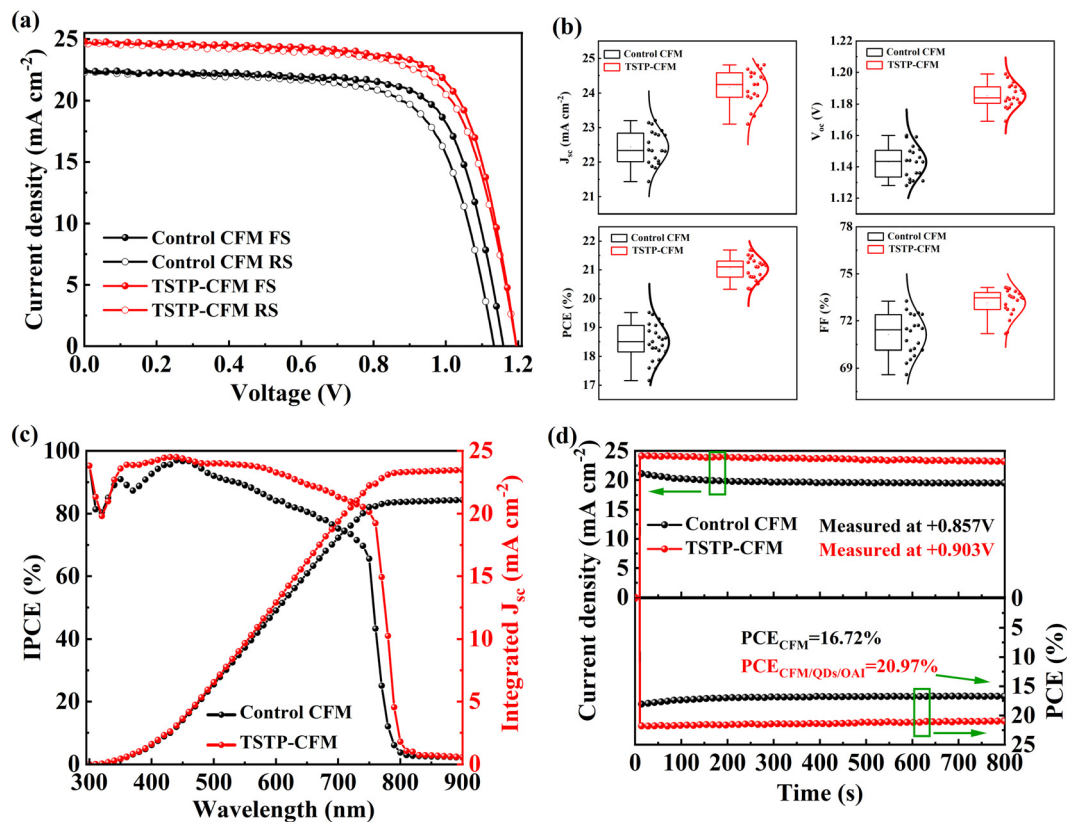
Fig. 4 (a) *J*–*V* curves, (b) statistical plots of *J*–*V* parameters, (c) IPCE and their integrated current density curves and (d) maximum power point tracking for 800 s in ambient air for the control CFM and TSTP-CFM devices.

Table 1 Performance parameters for FS and RS of the control CFM and TSTP-CFM devices. The hysteresis index (HI) has been determined using the equation of HI = (PCE$_{FS}$−PCE$_{RS}$)/PCE$_{FS}$.[14]

	V_{oc} (V)	J_{sc} (mA cm^{-2})	PCE (%)	FF	HI (%)
Control CFM FS	1.16	22.40	18.97	0.73	7.17
Control CFM RS	1.13	22.27	17.61	0.70	
TSTP-CFM FS	1.20	24.79	22.01	0.74	4.41
TSTP-CFM RS	1.20	24.70	21.04	0.71	

devices also demonstrate a similar increase as shown in Fig. 4b. The control devices yield an average PCE of 18.4% while the TSTP devices display a dramatically increased average PCE of 21.4%. In addition, the hysteresis index is reduced to 4.41% for the TSTP device from 7.17% for the control one. As shown in Fig. S5 and Table S2 (ESI†), PSCs with only M-QD or OAI treatment also exhibit a higher PCE than that of the control one, while weaker than that of the TSTP device. Fig. S6 (ESI†) shows the statistical distributions of the devices with only M-QD and OAI treatment, providing average PCEs of 20.3% and 20.1% for M-QDs and OAI treatment devices, respectively. These results indicate that the PSC performance can be improved by the one-step post-treatment and further enhanced by the TSTP strategy due to the multi-site passivation at the surface/interface/grain boundary of the perovskite film.

To testify the escalation in photo-current, the incident photon-to-current conversion efficiency (IPCE) measurement is carried out (Fig. 4c). A stronger spectral response in the range between 600–750 nm was observed for the TSTP device as compared with the control one, resulting in a higher integrated photo-current density calculated from the IPCE data (23.46 and 21.09 mA cm^{-2} for the device with/without TSTP treatment, respectively, which is consistent with the results from the *J*–*V* curves). Moreover, as shown in Fig. 4d, the TSTP device shows a stabilized PCE of 20.97% measured at the maximum power point for 800 s, while the control device shows a slow PCE decay trend under the same test conditions. Furthermore, to investigate the long-term stability of the devices, PCEs of the un-encapsulated device evolution as a function of time were recorded under three different conditions, namely, in air ($\sim$25 °C at $\sim$30% humidity) (denoted as C_1), in an N$_2$ environment at 85 °C (denoted as C_2) and in an N$_2$ environment under continuous light soaking (denoted as C_3). As shown in Fig. 5, the TSTP devices show remarkable stability, retaining over 90%, 75% and 80% of their initial PCEs after 2000 h of storage in C_1, C_2 and 1000 h of storage in C_3, respectively, which are much better than those of the control ones (all retaining less than 50%). The insets of Fig. 5a show that the water contact angles for TSTP and control perovskite films are 79° and 54°, respectively, confirming the greater hydrophobicity of the TSTP-CFM film, which acts as a shielding layer to resist moisture
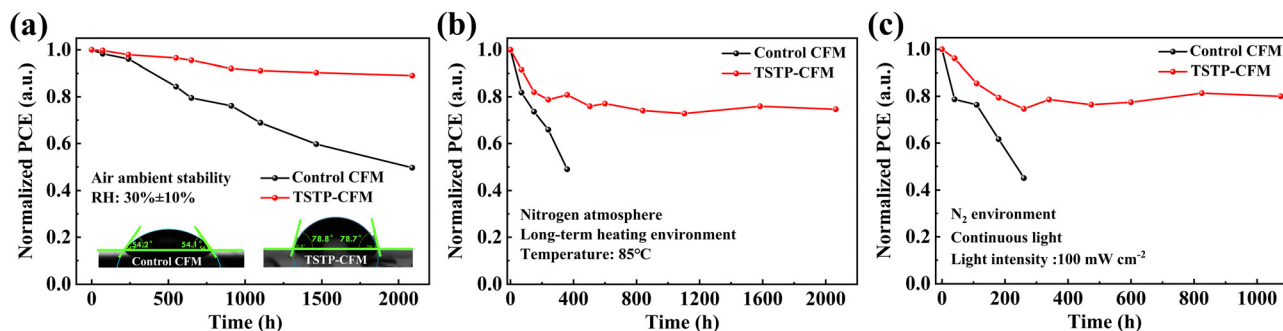
12702 | *J. Mater. Chem. C*, 2022, **10**, 12699–12707

This journal is © The Royal Society of Chemistry 2022

Fig. 5 Long-term stability of un-encapsulated devices based on the control CFM and TSTP-CFM (a) in air with a relative humidity of ∼30%, (b) in an N_2 environment at a constant temperature of 85 °C and (c) in an N_2 environment under continuous light soaking with 100 mW cm^{-2}.

infiltration and thereby suppresses PSC degradation. The greater hydrophobicity is attributed to the great hydrophobicity of the coated OLA on M-QDs and defect-reduced perovskite films.[36,44] Nevertheless, the better thermal and light stability of the TSTP device may have been caused by the stronger van der Waals interactions through dipole-dipole interactions or hydrogen bonding between the *n*-octylammonium cations and I/Br anions as indicated in previous publications,[45] resulting in the slowing down of the perovskite decomposition and improved device stability. In addition, as shown in Fig. S7 (ESI†), the long-term stability of the un-encapsulated devices with only M-QD and OAI treatment also exhibit better stability than the control one under the three test conditions mentioned above.

To investigate the charge recombination kinetics, the dependence of V_{oc} and J_{sc} on light intensity I measurements were carried out. Fig. 6a shows a smaller slope for the TSTP-CFM device (1.05 KT/e) than that for the control device (1.72 KT/e) from the V_{oc} *versus* ln(I) plots, indicating that there are fewer defect densities and reduced non-radiative recombination in TSTP-CFM PSCs. Similarly, the dependence of ln(J_{sc}) on ln(I) (Fig. 6b) shows a slope closer to 1 for the TSTP-CFM device (0.95) as compared with that of the control device (0.89), implying fewer defect densities and thus a more suppressed charge recombination in TSTP-CFM PSCs.[28,44–46] To evaluate the interfacial charge density and the relationship between the V_{oc} and built-in potential (V_{bi}) in PSCs, the classical
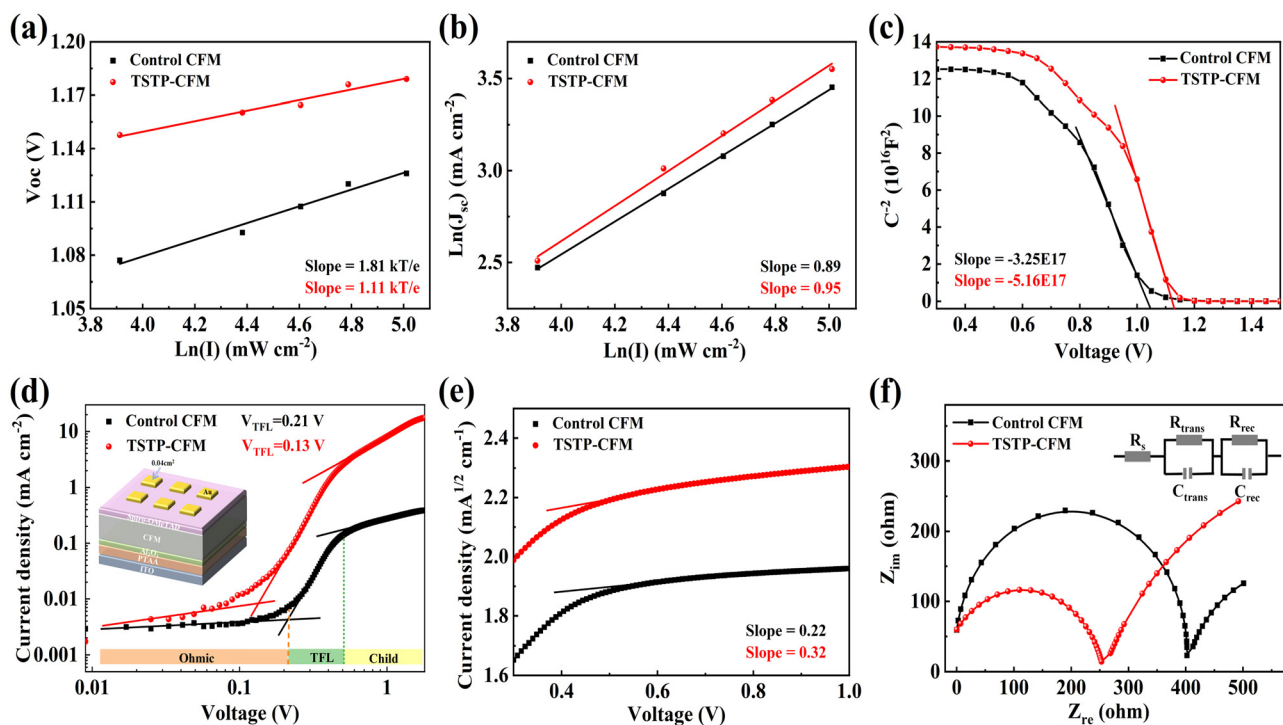

Fig. 6 (a) V_{oc} and (b) J_{sc} *versus* light intensity and (c) M−S plots of the control CFM and TSTP-CFM devices. (d) J−V and (e) $J^{1/2}$−V characteristics of SCLC measurements for hole-only devices with the architecture of ITO/PTAA/CFM (with and without TSTP treatment)/spiro-OMeTAD/Au; the inset is the device structure diagram. (f) EIS of the control CFM and TSTP-CFM devices under the illumination of 100 mW cm^{-2}; the inset shows the equivalent electrical circuit of PSCs.

Mott–Schottky (M–S) relation *via* the capacitance–voltage (*C–V*) measurements is investigated.[46,47] As shown in Fig. 6c, the V_{bi} values at the intercept $C^{-2} = 0$ are 1.03, and 1.12 V for the control and TSTP-CFM devices, respectively. The higher V_{bi} displayed by the TSTP-CFM devices indicates that the built-in band alignment contributes to a stronger charge separation capability, improving the trap passivation effect and enhancing the photogenerated carrier collection of the hole transport layer (HTL). In addition, a lower interfacial charge density is detected in the TSTP-CFM device as compared with the control one, which resulted from the inversely proportional relationship to the slope in the linear regime, indicating the faster charge transfer at the TSTP-CFM/HTL interface.[48–50] In contrast, the TSTP device exhibits a larger V_{bi} and fewer residual charges at the CFM/HTM interface, consistent with V_{oc} and J_{sc} trends (Fig. 4a).

The space-charge-limited current (SCLC) technique is used to quantize the effect of passivation on the trap density (n_{trap}).[51] The SCLC measurements are conducted by the dark *J–V* curves of the hole-only devices with the structure ITO/PTAA/CFM (with and without TSTP treatment)/spiro-OMeTAD/Au. As shown in Fig. 6d, the trap-filled limit voltage (V_{TFL}) can be found *via* the cross point of the fitting curves between the ohmic region and trap-filling region. The n_{trap} can be calculated according to the equation of $n_{trap} = 2V_{TFL}\varepsilon_r\varepsilon_0/eL^2$, where ε_0 and ε_r represent the vacuum permittivity and relative dielectric constant of the perovskite layer, *e* is the elementary charge and *L* is the thickness of the perovskite layer (about 500 nm determined by cross-section SEM).[52–54] The n_{trap} of the TSTP-treated device (2.70×10^{15} cm^{-3}) is lower than that of the untreated one (4.36×10^{15} cm^{-3}), indicating a decrease in the surface trap density after the TSTP treatment. Moreover, benefiting from the SCLC model at a high voltage, $J^{1/2}$–V curves are analyzed (Fig. 6e), and the hole mobility (μ_h) can be calculated by the Mott–Gurney law of $J = (9/8)\varepsilon_r\varepsilon_0\mu_h V^2 L^{-3}$.[54] The μ_h of the TSTP-treated device (2.73×10^{-3} cm^2 V^{-1} S^{-1}) is larger than that of the untreated one (1.29×10^{-3} cm^2 V^{-1} S^{-1}), mainly due to the decreased trap density. The decreased n_{trap} and enhanced μ_h in the TSTP-based device suggest that the TSTP strategy could efficiently passivate the defects of the perovskite layer, thus leading to the performance improvement of PSCs.

Electrochemical impedance spectroscopy (EIS) measurements have been employed to further investigate the charge transfer and recombination kinetics in PSCs. The measured EIS results are illustrated in Fig. 6f, and the fitted parameters are listed in Table S3 (ESI†). R_s is the series resistance. The first arc in the high-frequency region and the second arc in the low-frequency region correspond to the charge transfer impedance (R_{trans}) and charge recombination impedance (R_{rec}) in the device, respectively.[51,55] As seen from Table S3 (ESI†), the TSTP-based device shows a smaller R_{trans} of 282.8 Ω and a larger R_{rec} of 891.9 Ω as compared with 400.7 Ω and 365.8 Ω for the control devices, respectively, indicating more efficient charge transfer and fewer carrier recombination losses. To support this explanation, the dark *J–V* plots of PSCs with and without the TSTP treatment are obtained. As shown in Fig. S8 (ESI†), the TSTP-treated PSC exhibits a lower leakage current, suggesting more suppressed defects and less carrier recombinations,[56,57] thus resulting in better charge transfer through the transport layers, which is in agreement with the higher V_{oc}.

3. Conclusions

In summary, we have developed an effective TSTP strategy to increase both the PCE and stability of PSCs, in which M-QDs and OAI were used to treat the perovskite film sequentially. With the help of M-QDs and trace DMF in the first passivation solution, the grain boundaries of the perovskite films were caulked and became fuzzy. The perovskite surfaces were further passivated by OAI in the second treatment process. By employing this strategy, a high V_{oc} of 1.20 V and an optimization PCE of 22.01% were achieved by the TSTP-based PSCs. Moreover, the TSTP-based PSCs without encapsulation displayed excellent stability not only in air (~ 25 °C at ~ 30% humidity) but also in an N_2 environment at 85 °C or under continuous light soaking, still maintaining more than 90%, 75% and 80% of their initial efficiency storage over 2000 h, 2000 h and 1000 h, respectively. Our research provides a promising route for improving the performance and stability of PSCs by the TSTP strategy.

4. Experimental section

Materials

Tin oxide (SnO₂, 15 wt% in H₂O colloidal dispersion) was purchased from Alfa Aesar. Potassium chloride (KCl, 99%), potassium fluoride (KF, 99.9%), cesium iodide (CsI, 99.999%,), lead bromide (PbBr₂, 99.9%), oleylamine (OLA, 99.5%) and oleic acid (OA, 99.5%) were purchased from Aladdin. Indium tin oxide-coated glass slides (ITO, 15 Ω square^{-1}), methyl ammonium bromide (MABr, 99.9%), lead iodide (PbI₂, 99.99%), formamidine iodide (FAI, 99.9%), methylammonium iodide (MAI, 99. 9%) and 2,2',7,7'-tetrakis (*N,N* dimethoxyphenylamino)-9,9'-spirobi-fluorene (spiro-OMeTAD, 98.6%) were purchased from Advanced Electronic Technology Co., Ltd. Bis(trifluoromethanesulfonyl) imide salt (Li-TFSI, 99.9%), 4-*tert*-butylpyridine (^{t}BP, 98%), *N,N*-diethylformamide (DMF, 99%), dimethyl sulfoxide (DMSO, 99%) and *n*-octylammonium iodide (OAI, 99.5%) were purchased from Sigma-Aldrich. Gold (Au, 99.999%) was purchased from China New Metal Materials Technology Co.

Synthesis of M-QD solution

First, 0.44 mmol MABr and 0.44 mmol PbBr₂ were dissolved in 1 mL DMF and stirred for 30 min at 60 °C. Then, 40 µL of OLA was added and stirred for 10 min at room temperature to obtain a clarified solution, which was denoted as solution-A. Second, 180 µL of OA was added into 8 mL toluene solution under vigorous stirring for 30 min at room temperature to obtain the solution-B. Third, during the continuous vigorous stirring of solution-B, 0.5 mL of solution-A was added and the color of the mixed solution changed to yellow instantly. Finally,

the M-QD solution of the green supernatant, which was used to passivate perovskite films in the first step, was obtained after being centrifuged at 4000 rpm for 20 min. It is worth noting that a certain amount of DMF was present in the M-QD solution. The concentration of M-QDs in the green solution was quantified by the following method. Firstly, a clean dish was weighed. Secondly, 2 mL of the green supernatant was dropped onto the dish and dried naturally to obtain the M-QD solids. Finally, the dish containing M-QD solids was weighed again. The D-value between the two weighed results is the mass of the M-QDs, which is about 8.8 mg. Therefore, the concentration of M-QDs was inferred to be about 9 mM.

Solution preparation

The SnO$_2$ colloidal dispersion (15 wt%) was diluted to 10 wt% with a KCl aqueous solution (5 mg mL^{-1}) under stirring for 30 min to obtain the SnO$_2$–KCl solution. A perovskite precursor solution was prepared by mixing CsI (18.2 mg), MAI (31.7 mg), FAI (194.5 mg), PbBr$_2$ (115.6 mg) and PbI$_2$ (500.2 mg) powders in 1 mL DMF and DMSO (8.5 : 1.5, v/v) with stirring for 12 h in a nitrogen glovebox. The obtained M-QD green solution was diluted to 0.3 mM with toluene for standby. The HTM solution was obtained by dissolving spiro-OMeTAD (72.5 mg) in chlorobenzene (1 mL) containing 28.5 μL ^{t}BP and 18 μL Li-TFSI acetonitrile (520 mg mL^{-1}) with stirring for 12 h in a nitrogen glovebox. All solutions were filtered through a 0.2 μm syringe filter before spin-coating.

Film and device fabrication

The etched ITO was ultrasonically cleaned in glass cleaner, deionized water, acetone and ethanol for 20 min each, dried in a nitrogen flow and then treated in ultraviolet ozone (UVO) cleaner for 20 min. The electronic transmission layer (ETL) was prepared by spin-coating SnO$_2$–KCl solution onto the cleaned ITO substrate at 5500 rpm for 10 s, followed by annealing at 150 °C for 10 min and then treated with UVO for 60 min. The samples were transferred into an N$_2$ glovebox (O$_2$ < 0.01 ppm, H$_2$O < 0.01 ppm), on which a KF aqueous solution (0.5 mg mL^{-1}) was spin-coated at 3000 rpm for 10 s and annealed at 120 °C for 10 min (denoted as ITO/SnO$_2$–KCl/KF). In the N$_2$ glovebox, the perovskite layers were deposited on the ITO/SnO$_2$–KCl/KF substrates by spin-coating the perovskite precursor solution at 1000 rpm and 4500 rpm for 5 and 20 s, respectively. During the last 5 s of spin-coating, 1000 μL of diethyl ether antisolvent was drop-casted. The perovskite film was immediately annealed on a hotplate at 120 °C for 10 min and then cooled to room temperature. The passivation layers were prepared by successively spin coating the M-QD solution at 5000 rpm for 30 s and OAI isopropanol solution (2 mg mL^{-1}) at 5000 rpm for 30 s on the as-prepared perovskite films without any further heat treatment. subsequently, 30 μL of the HTM solution was deposited on the as-prepared passivation layer at 4500 rpm for 20 s. Finally, an 80 nm Au electrode was formed by thermal evaporation through a metallic mask, which determined the device working area of 4 mm^2.

Characterization

SEM, AFM and TEM measurements were performed on a JSM7001F field-emission scanning electron microscope (Japan Electron Optics Laboratory Co., Japan), a Multimode8 atomic force microscope (Bruker, USA) and a JEOL JEM-F200 transmission electron microscope (Nippon Electronics Co., Japan), respectively. XRD patterns were obtained on a DX-2700 X-ray diffractometer (Dandong Haoyuan, China). UV-vis absorption spectra were recorded on a Cary 5000 ultraviolet/visible spectrophotometer (Agilent Technologies Co. Ltd., China). PL spectra and TRPL decay dynamics were measured on a HORIBA Jobin Yvon Fluorolog-3 spectrofluorometer system and an FLS 980 PL spectrometer (Edinburgh Instrument, England) with Xe 900 (450 W xenon arc lamp) as the light source, respectively. The transient photovoltage spectrum was derived from a high-sensitivity surface photovoltage spectrometer test (Beijing China Education Au-Light Co., Ltd). J–V curves were obtained on a Keithley 2410 sourcemeter (Cleveland, OH, USA) at 100 mW cm^{-2} generated by a Newport 94043A solar simulator (USA) and calibrated with a certified silicon solar cell (Japanese Industrial Standards), including forward scans (FS, from −0.05 to 1.25 V) and reverse scans (RS, from 1.25 to −0.05 V). IPCE spectra were recorded on a Qtest Station 500ADX quantum efficiency test system (United States Dawn Technology Co. Ltd., USA). The water contact angle was characterized using a LAUDA OSA100 fiber optical contact angle tensiometer (LAUDA Scientific GmbH, China). MS, SCLC, and EIS measurements were characterized on a CHI660E electrochemical workstation (Chenhua Equipment Company, Shanghai, China). The impedance spectrum was simulated using the Z-View software.

Author contributions

Y. Feng performed the materials synthesis, device fabrications and characterizations. F. Li and Y. Feng co-wrote the first draft. R. Liu, Y. Rong and M. Wang contributed to the materials synthesis and characterizations. M. Jin and Q. Du contributed to the fabrications of films and devices. Z. Shen and Y. Liu contributed to the discussion of this concept. H. Hu and Y. Li measured the SCLC, PL and TRPL. All the authors approved the manuscript, discussed the results and commented on the manuscript. F. Li, H. Li and C. Chen co-directed this study.

Conflicts of interest

There are no conflicts of interest to declare.

Acknowledgements

This journal is © The Royal Society of Chemistry 2022

J. Mater. Chem. C, 2022, **10**, 12699–12707 | **12705**

References

1 F. Li, X. Deng, F. Qi, Z. Li, D. Liu, D. Shen, M. Qin, S. Wu, F. Lin, S. Jang, J. Zhang, X. Lu, D. Lei, C.-S. Lee, Z. Zhu and A. K. Y. Jen, *J. Am. Chem. Soc.*, 2020, **142**, 20134.

2 M. J. Jeong, K. M. Yeom, S. J. Kim, E. H. Jung and J. H. Noh, *Energy Environ. Sci.*, 2021, **14**, 2419.

3 P. Wang, R. Li, B. Chen, F. Hou, J. Zhang, Y. Zhao and X. Zhang, *Adv. Mater.*, 2020, **32**, 1905766.

4 N. J. Jeon, H. Na, E. H. Jung, T. Yang, Y. G. Lee, G. Kim, H.-W. Shin, S. I. Seok, J. Lee and J. Seo, *Nat. Energy*, 2018, **3**, 682.

5 Best research-cell efficiency chart, 2021. **https://www.nrel.gov/pv/cell-efficiency.html**.

6 A. Kojima, K. Teshima, Y. Shirai and T. Miyasaka, *J. Am. Chem. Soc.*, 2009, **131**, 6050.

7 W. Hui, L. Chao, H. Lu, F. Xia, Q. Wei, Z. Su, T. Niu, L. Tao, B. Du, D. Li, Y. Wang, H. Dong, S. Zuo, B. Li, W. Shi, X. Ran, P. Li, H. Zhang, Z. Wu, C. Ran, L. Song, G. Xing, X. Gao, J. Zhang, Y. Xia, Y. Chen and W. Huang, *Science*, 2021, **371**, 1359.

8 T. Bu, J. Li, H. Li, C. Tian, J. Su, G. Tong, L. K. Ono, C. Wang, Z. Lin, N. Chai, X. Zhang, J. Chang, J. Lu, J. Zhong, W. Huang, Y. Qi, Y. Cheng and F. Huang, *Science*, 2021, **372**, 1327.

9 R. Wang, T. Huang, J. Xue, J. Tong, K. Zhu and Y. Yang, *Nat. Photonics*, 2021, **15**, 411.

10 J. Chen, D. He and N.-G. Park, *Sol. RRL*, 2022, **6**, 2100767.

11 L. Zhu, X. Zhang, M. Li, X. Shang, K. Lei, B. Zhang, C. Chen, S. Zheng, H. Song and J. Chen, *Adv. Energy Mater.*, 2021, **11**, 2100529.

12 J. Xie, K. Yan, H. Zhu, G. Li, H. Wang, H. Zhu, P. Hang, S. Zhao, W. Guo, D. Ye, L. Shao, X. Guan, T. Ngai, X. Yu and J. Xu, *Sci. Bull.*, 2020, **65**, 1726.

13 L. Xie, P. Vashishtha, T. M. Koh, P. C. Harikesh, N. F. Jamaludin, A. Bruno, T. J. N. Hooper, J. Li, Y. F. Ng, S. G. Mhaisalkar and N. Mathews, *Adv. Mater.*, 2020, **32**, 2003296.

14 J. Peng, J. I. Khan, W. Liu, E. Ugur, T. Duong, Y. Wu, H. Shen, K. Wang, H. Dang, E. Aydin, X. Yang, Y. Wan, K. J. Weber, K. R. Catchpole, F. Laquai, S. De Wolf and T. P. White, *Adv. Energy Mater.*, 2018, **8**, 1801208.

15 P. Liu, Z. Liu, C. Qin, T. He, B. Li, L. Ma, K. Shaheen, J. Yang, H. Yang, H. Liu, K. Liu and M. Yuan, *Sol. Energy Mater. Sol. Cells*, 2020, **212**, 110555.

16 X. Li, C. Chen, M. Cai, X. Hua, F. Xie, X. Liu, J. Hua, Y. Long, H. Tian and L. Han, *Adv. Energy Mater.*, 2018, **8**, 1800715.

17 X. Zhu, M. Du, J. Feng, H. Wang, Z. Xu, L. Wang, S. Zuo, C. Wang, Z. Wang, C. Zhang, X. Ren, S. Priya, D. Yang and S. Liu, *Angew. Chem., Int. Ed.*, 2021, **60**, 4238.

18 E. Akman and S. Akin, *Adv. Mater.*, 2021, **33**, 2006087.

19 Y. Gao, Y. Wu, H. Lu, C. Chen, Y. Liu, X. Bai, L. Yang, W. Yu, Q. Dai and Y. Zhang, *Nano Energy*, 2019, **59**, 517.

20 Y. Weng, Z. Shen, M. Guo, F. Wu, F. Li, L. Zhu, L. Ling and C. Chen, *J. Mater. Chem. C*, 2019, **7**, 11559.

21 Z. Fang, L. Jia, N. Yan, X. Jiang, X. Ren, S. Yang and S. Liu, *InfoMat*, 2022, **4**, 12307.

22 C. F. Arias-Ramos, Y. Kumar, P. G. Abrego-Martinez and H. Hu, *Sol. Energy Mater. Sol. Cells*, 2020, **215**, 110625.

23 J. Song, Y. Yang, Y. Zhao, M. Che, L. Zhu, X. Gu and Y. Qiang, *Mater. Sci. Eng. B-Adv.*, 2017, **217**, 18.

24 J. Li, J. Ma, J. Hu, D. Wang and L. Wan, *ACS Appl. Mater. Interfaces*, 2016, **8**, 26002.

25 Z. Yao, W. Zhao, Z. Xu, J. Wen and S. Liu, *Small*, 2020, **16**, 2003582.

26 S. Xiao, Y. Bai, X. Meng, T. Zhang, H. Chen, X. Zheng, C. Hu, Y. Qu and S. Yang, *Adv. Funct. Mater.*, 2017, **27**, 1604944.

27 X. Li, G. Wu, M. Wang, B. Yu, J. Zhou, B. Wang, X. Zhang, H. Xia, S. Yue, K. Wang, C. Zhang, J. Zhang, H. Zhou and Y. Zhang, *Adv. Energy Mater.*, 2020, **10**, 2001832.

28 Q. Jiang, Y. Zhao, X. Zhang, X. Yang, Y. Chen, Z. Chu, Q. Ye, X. Li, Z. Yin and J. You, *Nat. Photonics*, 2019, **13**, 460.

29 N. Li, Z. Zhu, Q. Dong, J. Li, Z. Yang, C.-C. Chueh, A. K. Y. Jen and L. Wang, *Adv. Mater. Interfaces*, 2017, **4**, 1700598.

30 P. Chen, Y. Bai, S. Wang, M. Lyu, J. Yun and L. Wang, *Adv. Funct. Mater.*, 2018, **28**, 1706923.

31 Y. Cho, A. M. Soufiani, J. Yun, J. Kim, D. S. Lee, J. Seidel, X. Deng, M. A. Green, S. Huang and A. W. Y. Ho-Baillie, *Adv. Energy Mater.*, 2018, **8**, 1703392.

32 D. Lin, X. Xu, T. Zhang, N. Pang, J. Wang, H. Li, T. Shi, K. Chen, Y. Zhou, X. Wang, J. Xu, P. Liu and W. Xie, *Nano Energy*, 2021, **84**, 105893.

33 H. Kim, S.-U. Lee, D. Y. Lee, M. J. Paik, H. Na, J. Lee and S. I. Seok, *Adv. Energy Mater.*, 2019, **9**, 1902740.

34 S. M. Yoon, H. Min, J. B. Kim, G. Kim, K. S. Lee and S. I. Seok, *Joule*, 2021, **5**, 183.

35 W. Wu, J. Zhong, J. Liao, C. Zhang, Y. Zhou, W. Feng, L. Ding, L. Wang and D. Kuang, *Nano Energy*, 2020, **75**, 104929.

36 C. Chen, F. Li, L. Zhu, Z. Shen, Y. Weng, Q. Lou, F. Tan, G. Yue, Q. Huang and M. Wang, *Nano Energy*, 2020, **68**, 104313.

37 S. Kim, J. Kim, P. Ramming, Y. Zhong, K. Schoetz, S. J. Kwon, S. Huettner, F. Panzer and N.-G. Park, *Nat. Commun.*, 2021, **12**, 1554.

38 T. Zhou, H. Lai, T. Liu, D. Lu, X. Wan, X. Zhang, Y. Liu and Y. Chen, *Adv. Mater.*, 2019, **31**, 1901242.

39 W. Zhou, S. Chen, Y. Zhao, Q. Li, Y. Zhao, R. Fu, D. Yu, P. Gao and Q. Zhao, *Adv. Funct. Mater.*, 2019, **29**, 1809180.

40 H. Lu, Y. Liu, P. Ahlawat, A. Mishra, W. R. Tress, F. T. Eickemeyer, Y. Yang, F. Fu, Z. Wang, C. E. Avalos, B. I. Carlsen, A. Agarwalla, X. Zhang, X. Li, Y. Zhan, S. M. Zakeeruddin, L. Emsley, U. Rothlisberger, L. Zheng, A. Hagfeldt and M. Gratzel, *Science*, 2020, **370**, 74.

41 D. Wang, Z. Zhang, J. Liu, Y. Zhang, K. Chen, B. She, B. Liu, Y. Huang, J. Xiong and J. Zhang, *ACS Appl. Mater. Interfaces*, 2021, **13**, 45435.

42 Z. Li, B. Li, X. Wu, S. A. Sheppard, S. Zhang, D. Gao, N. Long and Z. Zhu, *Science*, 2022, **376**, 416.

43 R. Lin, J. Xu, M. Wei, Y. Wang, Z. Qin, Z. Liu, J. Wu, K. Xiao, B. Chen, S. M. Park, G. Chen, H. R. Atapattu, K. R. Graham, J. Xu, J. Zhu, L. Li, C. Zhang, E. H. Sargent and H. Tan, *Nature*, 2022, **603**, 73.

44 J. Zheng, F. Li, C. Chen, Q. Du, M. Jin, H. Li, M. Ji and Z. Shen, *ACS Appl. Mater. Interfaces*, 2022, **14**, 2989.

45 L. Quan, M. Yuan, R. Comin, O. Voznyy, E. M. Beauregard, S. Hoogland, A. Buin, A. R. Kirmani, K. Zhao, A. Amassian, D. H. Kim and E. H. Sargent, *J. Am. Chem. Soc.*, 2016, **138**, 2649.

46 F. Li, Z. Shen, Y. Weng, Q. Lou, C. Chen, L. Shen, W. Guo and G. Li, *Adv. Funct. Mater.*, 2020, **30**, 2004933.

47 Q. Du, Z. Shen, C. Chen, F. Li, M. Jin, H. Li, C. Dong, J. Zheng, M. Ji and M. Wang, *Sol. RRL*, 2021, **5**, 2100622.

48 Y. Ma, S. Zhang, Y. Yi, L. Zhang, R. Hu, W. Liu, M. Du, L. Chu, J. Zhang, X. Li, R. Xia and W. Huang, *J. Mater. Chem. C*, 2022, **10**, 5922.

49 T. Niu, Y. Xie, Q. Xue, S. Xun, Q. Yao, F. Zhen, W. Yan, H. Li, J. Bredas, H. Yip and Y. Cao, *Adv. Energy Mater.*, 2022, **12**, 2102973.

50 O. Almora, C. Aranda, E. Mas-Marza and G. Garcia-Belmonte, *Appl. Phys. Lett.*, 2016, **109**, 173903.

51 X. Deng, F. Li, Q. Wang, D. Liu, F. Lin, D. Shen, D. Lei, Y. Peng, Z. Zhu and A. K. Y. Jen, *Matter*, 2021, **4**, 3301.

52 J. Zheng, L. Zhu, Z. Shen, F. Li, L. Ling, H. Li and C. Chen, *Int. J. Min. Met. Mater.*, 2022, **29**, 283.

53 H. Chen, Q. Luo, T. Liu, J. Ren, S. Li, M. Tai, H. Lin, H. He, J. Wang and N. Wang, *Small*, 2019, **15**, 1904372.

54 M. Ji, M. Jin, Q. Du, J. Zheng, Y. Feng, Z. Shen, F. Li, H. Li and C. Chen, *ACS Appl. Energy Mater.*, 2021, **4**, 11144.

55 J. Du, C. Qiu, S. Li, W. Zhang, W. Zhang, Y. Wang, Z. Qiu, Q. Wang, K. Yang, A. Mei, Y. Rong, Y. Hu and H. Han, *Adv. Energy Mater.*, 2022, **12**, 2102229.

56 B. Wang, N. Li, L. Yang, C. Dall'Agnese, A. K. Jena, S.-I. Sasaki, T. Miyasaka, H. Tamiaki and X. Wang, *J. Am. Chem. Soc.*, 2021, **143**, 2207.

57 G. Liu, H. Zheng, X. Xu, S. Xu, X. Zhang, X. Pan and S. Dai, *Adv. Funct. Mater.*, 2019, **29**, 1807565.

This journal is © The Royal Society of Chemistry 2022

J. Mater. Chem. C, 2022, **10**, 12699–12707 | **12707**